IEEE Access
Multidisciplinary | Rapid Review | Open Access Journal

Received December 17, 2019, accepted January 15, 2020, date of publication January 27, 2020, date of current version February 5, 2020.

Digital Object Identifier 10.1109/ACCESS.2020.2969497

Adaptive Caging Configuration Design Algorithm of Hyper-Redundant Manipulator for Dysfunctional Satellite Pre-Capture

WENYA WAN, CHONG SUN, AND JIANPING YUAN
National Key Laboratory of Aerospace Flight Dynamics, Northwestern Polytechnical University, Xi'an 710072, China
Corresponding author: Chong Sun (sunchong@nwpu.edu.cn)

This work was supported by the National Natural Science Foundation of China under Grant 11802238.

ABSTRACT This paper presents an adaptive caging configuration design algorithm of the hyper-redundant manipulator for dysfunctional satellite pre-capture. Taking advantages of the extreme flexibility and hyper-redundancy, the hyper-redundant manipulator wraps its whole body around the dysfunctional satellite to restrain its motion without requiring grappling points and accurate information. However, the hyper-redundancy also makes the caging configuration design more complicated and challenging. In this paper, the dynamic sequential caging following algorithm based on rapidly-exploring random tree algorithm is proposed to search the caging configuration in real-time. First, according to the discretized caging trace, which is twining around the grasped object and selected based on the caging conditions, the joints of the hyper-redundant manipulator are divided into several groups in advance. Then, the joint angles are searched group by group to realize the match of the discretized caging trace by the hyper-redundant manipulator. As a result, the configuration between the grasped object and the hyper-redundant manipulator satisfies the caging conditions. The main advantages of the proposed caging motion planning algorithm lie in the avoidance of the inversion and the efficiency of computation. Finally, the pre-capture of two dysfunctional satellites with different shapes using a twenty universal joint manipulator is implemented, and the simulation results verify the efficiency of the proposed method.

INDEX TERMS Caging configuration design, hyper-redundant manipulator, caging trace, dynamic sequential caging following algorithm, rapidly-exploring random tree.

I. INTRODUCTION

Due to running out of fuel, attitude and orbit control system failure, task termination, and so on, there are more and more dysfunctional satellites in space. These dysfunctional satellites not only occupy valuable orbital resources but also threaten the safety of operational satellites [1]. Conceptually, many methods for grasping dysfunctional satellites have been proposed, such as space manipulator capturing [2] and net capturing [3], [4]. As discussed in the reference [1], advantages and drawbacks exist in any of these options. The choice of dysfunctional satellite capture method should be dependent on the concrete mission scenario. To improve the economic benefits, on-orbit maintenance of dysfunctional satellites seems to be the best choice. In this case, the ability to grasp and operate the dysfunctional satellite is necessary. Based on this background, the space manipulator seems to be a better choice due to its controllability. In practice, space robotic systems with manipulators play a more and more important role in on-orbit servicing, such as docking, berthing, repairing, upgrading, transporting, rescuing, and orbital debris removal [5]–[7].

A hyper-redundant manipulator has a greater number of degrees of freedom (DOFs) than a traditional manipulator, which makes it has extreme flexibility and well suited to work in highly constrained environments [8]–[10]. Taking advantages of the extreme flexibility and hyper-redundancy, an adaptive caging approach for dysfunctional satellite pre-capture using hyper-redundant manipulator is proposed in this paper. Specifically, similar as the trunk of an elephant [11], the hyper-redundant manipulator wraps its whole body around the grasped dysfunctional satellite to form an

The associate editor coordinating the review of this manuscript and approving it for publication was Zheng H. Zhu.

encirclement, which can restrain the dysfunctional satellite motion. Then, a good condition for grasping and manipulating the dysfunctional satellite is created, in which the dysfunctional satellite cannot escape from the encirclement formed by the hyper-redundant manipulator, even if there is unexpected collision between the dysfunctional satellite and the hyper-redundant manipulator. The most striking feature of caging is that it is assumed to be accomplished only by position-controlled agents without considering mechanical properties like contact and forces, which relaxes control during the caging process [12]–[14]. Therefore, compared with current dysfunctional satellite capturing and removal methods (e.g. [2]–[4], [15]), neither grappling points nor accurate information are required in our proposed method, which means requirements for the cooperative level of grasped object are lower. Actually, the shape and size of dysfunctional satellites are various, and the known information of dysfunctional satellites is usually limited, which create challenges for on-orbit servicing [1]. Concretely, in this paper, we focus on how to find an effective caging configuration of hyper-redundant manipulator that can restrict the dysfunctional satellite to a limited region, which belongs to the pre-capture phase.

However, due to higher DOFs, the configuration design of hyper-redundant manipulator becomes very complicated and challenging. The current researches in this field can be divided into three main categories: geometrical methods [16]–[18], numerical methods [19], [20] and artificial neural network methods [21]–[23]. The geometrical methods usually use a backbone function [16] or a mode function [10] to describe the configuration of hyper-redundant manipulator, in which the complexity of the solution and the computation of the inverse kinematics will be simplified to some degree. However, the validity of this kind of methods depends on the choice of backbone/mode function. In terms of the numerical methods, the generalized inverse of the Jacobian matrix is used to deal with the differential kinematics equations. However, the computational load will become very large with the increase of the number of DOFs, which affects the real-time control ultimately. As for the artificial neural network methods, they are used to solve the configuration planning problem of general manipulators recently with the development of artificial intelligence technology. However, similar to the numerical methods, with the increase of the number of DOFs, the size of the training set will change significantly that increases the computating complexity.

To solve this problem, the dynamic sequential caging following algorithm based on rapidly-exploring random tree (RRT) algorithm is proposed to search caging configuration of the hyper-redundant manipulator in real-time in this paper. The main idea of the proposed algorithm is adjusting the joint angles of the hyper-redundant manipulator sequentially. Concretely, according to the geometry of the grasped object, the joints of the hyper-redundant manipulator are divided into several groups in advance. Then, the joint angles are searched group by group using RRT algorithm [24] to realize the match of the hyper-redundant manipulator with the discretized caging trace. As a result, the configuration between the grasped object and the hyper-redundant manipulator satisfies the caging conditions. Therefore, not only does the inverse kinematics avoid where singularity usually occurs, but also the computation efficiency improves.

In this paper, caging conditions using the hyper-redundant manipulator are derived first through static analysis and dynamic analysis. The caging trace twining around the grasped object is introduced and quantified. Next, the caging motion planning algorithm is designed to track the caging trace with uncertainty by the hyper-redundant manipulator in real-time. In order to guarantee the effectiveness of the caging and the operability of the hyper-redundant manipulator, the caging trace is discretized into a sequence of critical points connected by caging edges. These critical points are targets for joints of the hyper-redundant manipulator to track. Then, the dynamic sequential caging following algorithm based on RRT algorithm searches feasible paths for joints to match with their corresponding critical points in real-time.

The rest of the paper is organized as follows. Section II describes the derivation of caging conditions of the hyper-redundant manipulator. Section III describes the caging motion planning algorithm of the hyper-redundant manipulator. In Section IV, a twenty universal joint manipulator caging two dysfunctional satellites with different shapes is chosen as examples to verify the effectiveness of the proposed method. Finally, conclusive remarks are given in Section V.

II. CAGING CONDITIONS OF THE HYPER-REDUNDANT MANIPULATOR

In this paper, the hyper-redundant manipulator uses its whole body to cage an object. Therefore, the essence of the hyper-redundant manipulator caging is to form an encircling trace around the grasped object as shown in Fig. 1. Here, we introduce the concept called ''caging trace'', which is located on the surface of the grasped object and surrounds around the grasped object to restrain its motion. Static and dynamic analysis of the caging condition derivation are discussed in the following parts. Considering the variety of the dysfunctional satellite geometries, we simplify the satellite as a prototype composed of a cuboid (mainbody) and two solar panels (attachment) only for the purpose of analysis (Fig. 2).

A. STATIC ANALYSIS

For the static analysis, the motion of the grasped object and the hyper-redundant manipulator, and the uncertainty of the grasped object are all ignored. We only focus on the relative constraint relationship between the caging trace and the grasped object, i.e., how to design a caging trace that could restrain the object's motion. To cage an object firmly and conveniently, the ideal case is that the caging trace is coincided with a specific closed curve located on the object's surface (such as the green solid closed lines shown in Fig. 2). Actually, the closed caging trace is hard to realize by the hyper-redundant manipulator subject to its structural

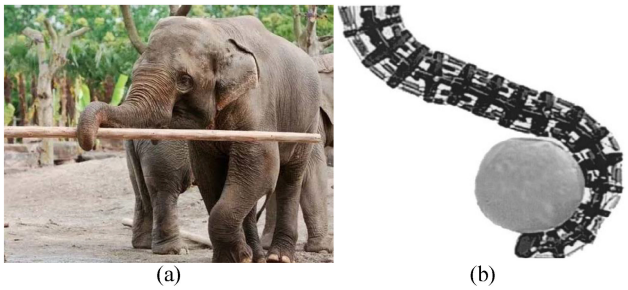

FIGURE 1. Illustration of the elephant trunk grasping objects. (a) The elephant trunk grasping a long stick. (b) The elephant trunk manipulator grasping a ball [25].

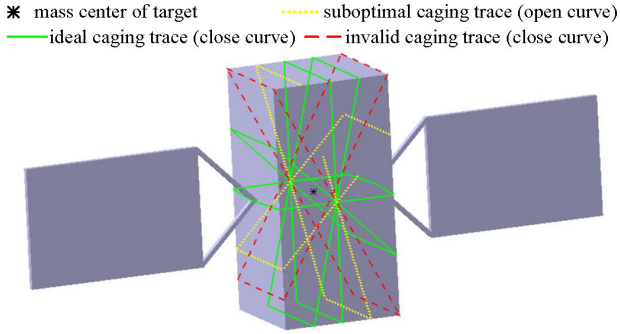

FIGURE 2. Illustration of the caging trace.

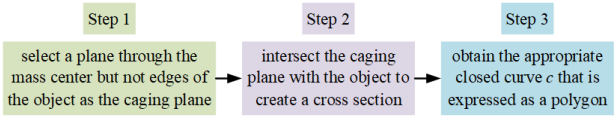

FIGURE 3. Steps of generating an appropriate closed curve.

constraints. In contrast, a suboptimal situation usually occurs where the caging trace is open and coincides with a part of the closed curve, but its opening length (or gap) is small enough to prevent the target from escaping (such as the yellow dotted open lines in Fig. 2). Thus, the caging trace design problem is transformed into how to select an appropriate closed curve located on the object's surface as the caging trace.

Different closed curves of an object can be obtained from different cross sections of the object. Fig. 3 shows steps of how to generate an appropriate closed curve c.

There are three steps in the whole procedure. The first step is to select the caging plane $\xi : f_\xi(x, y, z) = 0$. The reason to select the caging plane through the mass center but not edges of the object is to guarantee the robustness of a capture. As shown in Fig. 2, planes composed by green solid or yellow dotted lines are valid caging planes. However, planes consisting of red imaginary lines pass through the mass center and edges simultaneously are invalid because the manipulator will break the current configuration easily under external disturbance. In other words, contact points at edges are neutral static. The second step is to intersect the caging plane with the object to create a cross section λ.

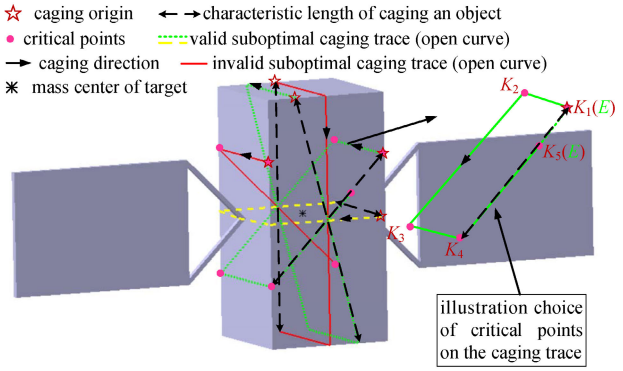

FIGURE 4. Illustration of additional requirements for the second case to realize a firm capture.

Assume the grasped object, denoted by O, consists of n_O faces $\beta = \{\beta_1, \beta_2, \cdots, \beta_{n_O}\}$ with equation $\beta_i : f_{\beta_i}(x, y, z) = 0 (i = 1, 2, \cdots, n_O)$. Then λ can be expressed as follows

$$\lambda = \xi \cap O \tag{1}$$

The last step is to find the closed curve c, which is the boundary of λ just as the green solid closed curves shown in Fig. 2. The compenent of c, denoted by c_i, can be expressed mathmatically as (2), then $c = \bigcap_{i=1}^{n_O} c_i$.

$$\begin{aligned} c_i &= \xi \cap \beta_i \\ &=: f_{c_i}(x, y, z) = f_\xi(x, y, z) - f_{\beta_i}(x, y, z) = 0 \\ &\qquad (i = 1, 2, \cdots, n_O) \end{aligned} \tag{2}$$

Next, we need to determine the caging trace η. As discussed before, the relationship between η and c satisfies

$$\eta \subseteq c \tag{3}$$

There are two cases for (3). The first one is $\eta = c$, which can guarantee a firm capture doubtlessly. The second one is $\eta \subset c$, i.e., η is a part of c, while the second case could not guarantee a 100% valid caging. Therefore, there are additional requirements for the second case to realize a firm caging. As shown in Fig. 4, the red solid curves are invalid because their gaps are too large to restrain the motion of the object, but the green dotted curves are valid because their gaps are small enough to prevent the object from escaping when there is external disturbance acting on the object. However, there are some special cases. For example, although the gap of the yellow imaginary curve is large, it is still valid because it utilizes the attachment of the grasped object to provide additional constraints.

In general, to guarantee a firm caging, the opening caging curve should be throughout the boundary of the cross section λ, such as the green dotted curves in Fig. 4. To describe additional requirements theoretically, the characteristic length, which is denoted by L_c, is introduced. Concretely, L_c is a specific edge of λ determined by the caging origin (the starting point on the caging trace for the hyper-redundant manipulator

to implement caging operation), the caging direction (the direction of the hyper-redundant manipulator to implement caging operation) and the geometry of the grasped object. As shown in Fig. 4, the double arrowhead imaginary lines represent the characteristic length of caging an object. Apparently, the gap of valid caging curves L_0 is less than L_c, which can be expressed as follows:

$$L_0 < L_c \tag{4}$$

Remark 1: The caging trace calculated here is ideal because it perfectly matches the geometry of the grasped object, which means that the hyper-redundant manipulator does not need to adjust its caging configuration to form a firm capture. There is no need for a full match of the caging trace with the hyper-redundant manipulator because caging is a loose closure strategy with certain margin and allows changing the size of a caging configuration within the margin [13].

Remark 2: The role of the attachments, such as solar panels, cannot be ignored. For one thing, these attachments can relax the caging conditions to some degree, which means that the opening caging curve may not need throughout the boundary of the cross section λ. For example, $L_0 = L_c$ is also a valid caging curve in some special cases if the attachment of the grasped object can provide constraints, such as the yellow imaginary curves in Fig. 4. For another, these attachments contribute to form a more stable caging configuration because of the additional restraints offered by them.

Last but not least, the caging trace is usually not unique. All the caging traces form a set Γ as shown in (5). η is a such trace that can restrain the motion of the grasped object.

$$\Gamma = \{\eta\} \tag{5}$$

B. DYNAMIC ANALYSIS

For the dynamic analysis, the motion of grasped objects, the motion of the hyper-redundant manipulator and the uncertainty of grasped objects should be taken into consideration. The real-time requirement of the dynamic analysis is inevitable due to the presence of the uncertainty of the grasped object. In addition, the collision is very likely to occur during the caging process, thus collision avoidance is necessary. Specifically, the dynamic analysis is throughout the caging track design and it will be discussed detailedly in subsection III-B.

III. CAGING TRACK DESIGN

The aim of caging motion planning is to realize the match of the caging trace with the hyper-redundant manipulator. Fig. 5 shows the task description of caging a dysfunctional satellite by the hyper-redundant manipulator, in which the hyper-redundant manipulator mounted on a serving satellite approaches the debris first, then it tracks a caging trace. For the convenience of study, the manipulator is converted into a chain structure composed of a series of straight segments.

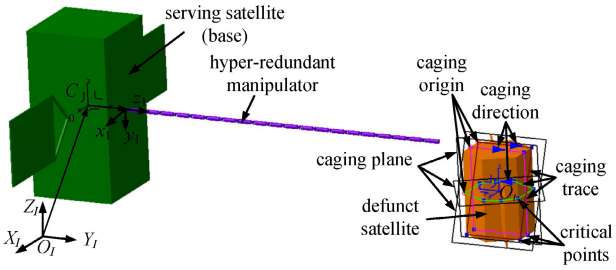

FIGURE 5. Task description of caging a dysfunctional satellite by the hyper-redundant manipulator.

TABLE 1. D–H parameters of the hyper-redundant manipulator.

Link i	$(\theta_i, \psi_i)[^\circ]$	$\alpha_i[^\circ]$	a_i[m]	d_i[m]
1	(0,0)	90	0	l_0
2	(0,0)	0	0	l_1
...	...	...	...	...
$n-1$	(0,0)	0	0	l_{n-2}
n	(0,0)	0	0	l_{n-1}

A. KINEMATIC MODEL OF THE HYPER-REDUNDANT MANIPULATOR

A hyper-redundant manipulator with n universal joint structure is adopted in this paper. The universal joint has two orthogonal DOFs. The kinematic model and the D-H parameters of the hyper-redundant manipulator are shown in Fig. 6 and listed in Table 1, respectively. For convenience of discussion, some symbols are defined in Table 2. For the body fixed frame of the jth link, denoted by $O_jx_jy_jz_j (j = 1, 2, \ldots, n)$, its origin O_j is fixed on the jth joint center, z_j axis is along the jth link directing the next adjacent joint center, x_j axis is along the vertical rotary shaft, and y_j axis is along the horizontal rotary shaft. Besides, $O_jx_jy_jz_j$ is the right-handed coordinate system. When the axes of all links are collinear and values of the rotation angle of all joints are 0°, all x_j or y_j axes are coplanar.

Remark 3: It should be pointed out that there is a little difference between the D-H parameters used in this paper and the traditional one [18], which is due to that each joint has two orthogonal DOFs. Specifically, there are five parameters to describe the transformation matrixes of two adjacent links: θ_j, ψ_j, α_i, a_i and d_i. As a result, the coordinate transformation matrix of two adjacent links also differs with the traditional one.

As shown in Fig. 6, there are three steps to obtain the coordinate transformation matrix from $O_jx_jy_jz_j$ to $O_{j-1}x_{j-1}y_{j-1}z_{j-1}$:

(1) $O_{j-1}x_{j-1}y_{j-1}z_{j-1}$ is shifted l_{j-1} along z_{j-1} axis, then a new coordinate frame system $O^1_{j-1}x^1_{j-1}y^1_{j-1}z^1_{j-1}$ is obtained;

(2) $O^1_{j-1}x^1_{j-1}y^1_{j-1}z^1_{j-1}$ rotates θ_{j-1} around y^1_{j-1} axis, then a new coordinate frame system $O^2_{j-1}x^2_{j-1}y^2_{j-1}z^2_{j-1}$ is obtained whose x^2_{j-1} axis coincides with x_j axis;

(3) $O^2_{j-1}x^2_{j-1}y^2_{j-1}z^2_{j-1}$ rotates ψ_{j-1} around $x^2_{j-1}(x_j)$ axis, then $O_jx_jy_jz_j$ is obtained.

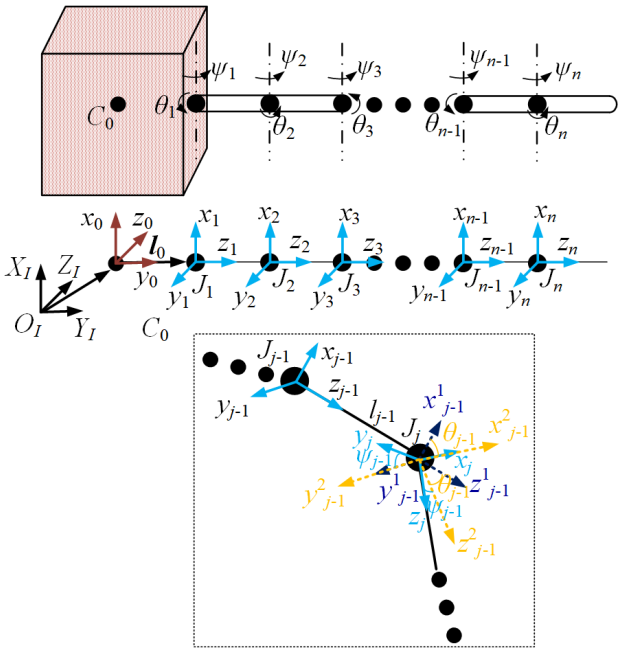

FIGURE 6. Kinematic model of the hyper-redundant manipulator.

TABLE 2. Some important symbols used in this paper.

Symbol	Representation
C_0	the mass center of servicing satellite
$\boldsymbol{l}_0$	the vector from C_0 to the first joint J_1
J_j	the jth joint, $j = 1, 2, \ldots, n$
l_j	the length of the jth link, $j = 1, 2, \ldots, n$
θ_j	the rotation angle about y_j axis of the jth joint, $j = 1, 2, \ldots, n$
ψ_j	the rotation angle about x_j axis of the jth joint, $j = 1, 2, \ldots, n$
$O_I X_I Y_j I Z_I$	the inertial coordinate system
$C_0 x_0 y_0 z_0$	the fixed coordinate system of the servicing satellite
$O_j x_j y_j z_j$	the fixed coordinate system of the jth joint and link, $j = 1, 2, \ldots, n$
${}^i\boldsymbol{T}_j$	the coordinate transformation matrix from $O_j x_j y_j z_j$ to $O_i x_i y_i z_i$

Therefore, the coordinate transformation matrix between two adjacent coordinate frames $O_j x_j y_j z_j$ and $O_{j-1} x_{j-1} y_{j-1} z_{j-1}$, can be obtained as:

$$\begin{aligned} {}^{j-1}T_j &= Trans(0, 0, l_{j-1}) \cdot Rot(y^1_{j-1}, \theta_{j-1}) \\ &\quad \cdot Rot(x^2_{j-1}, \psi_{j-1}) \\ &= \begin{bmatrix} c_\theta & s_\theta s_\psi & s_\theta c_\psi & 0 \\ 0 & c_\psi & -s_\psi & 0 \\ -s_\theta & c_\theta s_\psi & c_\theta c_\psi & l_{j-1} \\ 0 & 0 & 0 & 1 \end{bmatrix} \end{aligned} \tag{6}$$

where c_θ is short for $\cos\theta_{j-1}$; s_θ is short for $\sin\theta_{j-1}$; c_ψ is short for $\cos\psi_{j-1}$; s_ψ is short for $\sin\psi_{j-1}$; $Trans(x, y, z)$ is the translational transfer matrix expressed in (7); $Rot(y, \theta)$ is the rotational transfer matrix around y axis expressed in (8); $Rot(x, \psi)$ is the rotational transfer matrix around x axis

TABLE 3. Simulation Parameters of the caging ability test.

Parameters		Values
hyper-redundant manipulator	joint number	$n = 20$
	link length	l=0.2m
	joint angles range	$\theta_i \in [-180°, 180°]$
	joint angles range	$\psi_i \in [-180°, 180°]$
	initial joint angles	$\theta_{i0} = 0°$ and $\psi_{i0} = 0°$
caging trace 1	geometry	circle
	radius	r_c=0.6073m
caging trace 2	geometry	square
	side length	a_c=0.95m
caging direction	counterclockwise	

expressed in (9).

$$Trans(x, y, z) = \begin{bmatrix} 1 & 0 & 0 & x \\ 0 & 1 & 0 & y \\ 0 & 0 & 1 & z \\ 0 & 0 & 0 & 1 \end{bmatrix} \tag{7}$$

$$Rot(y, \theta) = \begin{bmatrix} \cos\theta & 0 & \sin\theta & 0 \\ 0 & 1 & 0 & 0 \\ -\sin\theta & 0 & \cos\theta & 0 \\ 0 & 0 & 0 & 1 \end{bmatrix} \tag{8}$$

$$Rot(x, \psi) = \begin{bmatrix} 1 & 0 & 0 & 0 \\ 0 & \cos\psi & -\sin\psi & 0 \\ 0 & \sin\psi & \cos\psi & 0 \\ 0 & 0 & 0 & 1 \end{bmatrix} \tag{9}$$

Therefore, the pose (position and attitude) of the jth link can be obtained according to (10).

$${}^I\boldsymbol{T}_j = {}^I\boldsymbol{T}_0 {}^0\boldsymbol{T}_1 {}^1\boldsymbol{T}_2 \cdots {}^{j-2}\boldsymbol{T}_{j-1} {}^{j-1}\boldsymbol{T}_j \tag{10}$$

where ${}^I\boldsymbol{T}_0$ is the coordinate transformation matrix from $C_0 x_0 y_0 z_0$ to $O_I X_I Y_j I Z_I$; ${}^0\boldsymbol{T}_1$ is the coordinate transformation matrix from $O_1 x_1 y_1 z_1$ to $C_0 x_0 y_0 z_0$.

The caging ability of the hyper-redundant manipulator to realize the match of a given caging trace is the basis of our proposed method, which is tested. The simulation parameters are shown in Table 3. Fig. 7 shows the caging process. Apparently, the hyper-redundant has the ability to match its shape with the given caging trace by adjusting its joint angles sequentially. The final joint angle values are shown in Table 4, and all the joint angles are located in the given range. Subject to the structural constraints, the hyper-redundnat manipulator cannot match the given circular trace perfectly. Alternatively, it forms an envelope around the circle.

Remark 4: The caging traces we chosen here are planar for simplicity. Thus, the desired caging configuration can be achieved through adjusting $\theta_i (i = 1, 2, \ldots, n)$. While, the proposed method can also be applied for spatial caging cases as each universal joint has two orthogonal DOFs.

B. CAGING MOTION PLANNING ALGORITHM

To simplify the problem without losing generality, several assumptions are made as follows:

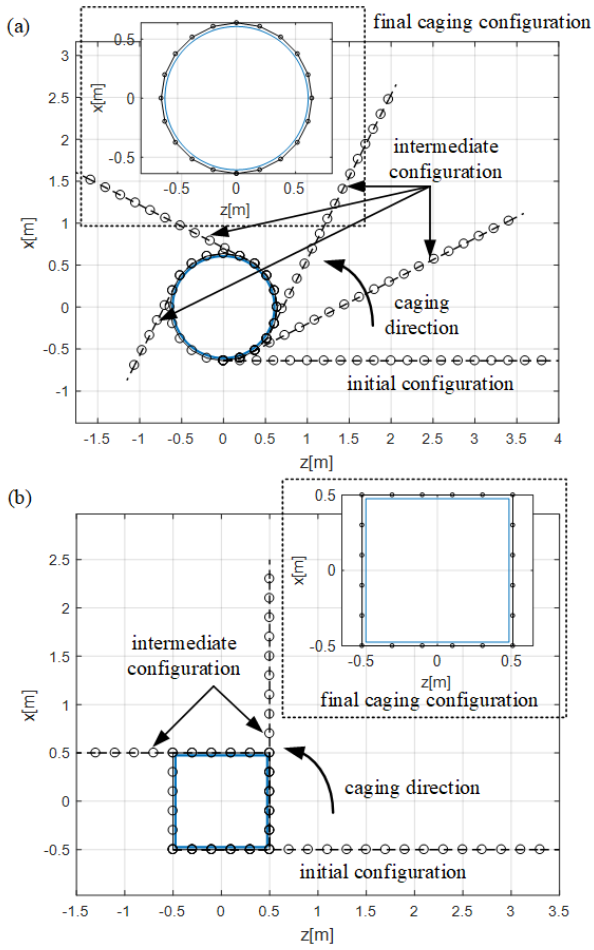

FIGURE 7. Simulation results of caging ability test. (a) The caging trace is a circle. (b) The caging trace is a square.

TABLE 4. Simulation results of caging ability test.

Joint angles [°]	Caging trace 1	Caging trace 2
(θ_1, ψ_1)	(9,0)	(0,0)
(θ_2, ψ_2)	(18,0)	(0,0)
(θ_3, ψ_3)	(18,0)	(0,0)
(θ_4, ψ_4)	(18,0)	(0,0)
(θ_5, ψ_5)	(18,0)	(0,0)
(θ_6, ψ_6)	(18,0)	(90,0)
(θ_7, ψ_7)	(18,0)	(0,0)
(θ_8, ψ_8)	(18,0)	(0,0)
(θ_9, ψ_9)	(18,0)	(0,0)
(θ_{10}, ψ_{10})	(18,0)	(0,0)
(θ_{11}, ψ_{11})	(18,0)	(90,0)
(θ_{12}, ψ_{12})	(18,0)	(0,0)
(θ_{13}, ψ_{13})	(18,0)	(0,0)
(θ_{14}, ψ_{14})	(18,0)	(0,0)
(θ_{15}, ψ_{15})	(18,0)	(0,0)
(θ_{16}, ψ_{16})	(18,0)	(90,0)
(θ_{17}, ψ_{17})	(18,0)	(0,0)
(θ_{18}, ψ_{18})	(18,0)	(0,0)
(θ_{19}, ψ_{19})	(18,0)	(0,0)
(θ_{20}, ψ_{20})	(18,0)	(0,0)

(a) The uncertainty of grasped objects, such as geometry parameters uncertainty, kinematic and dynamic parameters uncertainty, and inertial parameters uncertainty, is integrated to the uncertainty of the caging trace during the caging process. This is due to the direct performance of all these uncertainties is the caging trace uncertainty during the caging process.

(b) The hyper-redundant manipulator is in a fully expanding state before implementing the caging operation, i.e., initial values of joint angles are zero.

(c) The actuation sequence of joint angles is from the base to the tip during the caging process. Besides, the part close to the base of the hyper-redundant manipulator contacts the grasped object first.

(d) The orbital motion between the grasped object and the servicing satellite system is synchronous, and the relative distance between the grasped object and the hyper-redundant manipulator is very small, which means that we could only focus on the caging motion of the hyper-redundant manipulator.

(e) The motion and shape information of grasped target can be obtained from the servicing satellite through observation and estimation.

Assumption (e) is reasonable in practice, because many technologies have been put forward to estimate the state information of a space target [26], [27]. As the distance between the grasped object and the servicing satellite grows smaller and smaller, the measured information will be more and more accurate due to the improvement of the measurement accuracy. Thus, the uncertainty of the caging trace is assumed to be limited and the caging trace will also change towards a more realistic situation during the caging process.

The are three main steps of the whole caging motion planning algorithm, which will be described in detail in the following parts.

1) DETERMINING THE PROTOTYPE OF THE CAGING TRACE

Due to the uncertainty of the grasped non-cooperative target, it is very difficult to determine the accurate caging trace. Thus, the prototype of a caging curve is introduced, which is a reference caging trace obtained from the initial measuring geometry information of the grasped object. Concretely, the prototype of a caging trace can be calculated according to the static analysis in subsection II-A. The ideal situation is that there are no deviation between the prototypical caging trace and the actual caging trace. However, the actual caging trace is very likely to change as the caging operation is executed. There are two reasons for this phenomenon: 1) limited by the accuracy of the measuring instruments, the closer the servicing satellite is to the dysfunctional satellite, the more full-scale measurement of the dysfunctional satellite can be obtained, and the more accurate informtion of the dysfunctional satellite is achieved; 2) the complete attitude synchronization between the grasped non-cooperative target and the servicing satellite system is hard to realize owing to the non-cooperation of the grasped target. For simplicity, the attitude asynchronism is also processed into the uncertainty of the caging trace. Generally, the actual caging trace will not change too much during the caging process. In this paper, we assume it is changed based on the prototypical caging

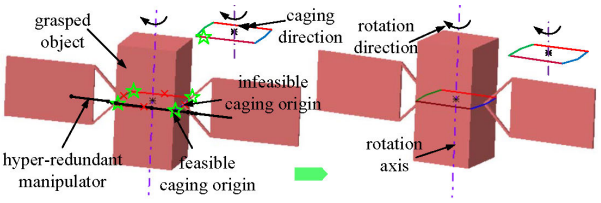

FIGURE 8. Illustration of the motion of the caging trace.

trace within a given threshold value. Noticeably, the caging trace is movable within a certain range as shown in Fig. 8.

Moreover, the prototypical caging traces for a specific grasped target form a set as shown in (5). Different caging trace corresponds to different tracking of the hyper-redundant manipulator. The random strategy is adopted, which means that the determination of the prototypical the caging trace is random, i.e., the generation of the caging plane is random; the type of the caging trace–closed or open, is also random; and if the caging trace is open, its gap is also random as long as it satisfies (4).

2) DETERMINING CAGING ELEMENTS

For convenience, the caging origin, the caging direction and the critical points are intergrated as caging elements. Considering the feasibility of the caging by the hyper-redundant manipulator, the caging origin is chosen as the intersection of the closed curve and the edge of the grasped object. As shown in Fig. 8, the points marked by five-pointed star are the feasible caging origins, while the points marked by cross are the infeasible caging origins. This is because the hyper-redundant manipulator is in a fully expanding state before implementing the caging operation as described in assumption (b), which means that the first contact point must be located on the edge of the grasped object. The caging direction is determined by the caging origin and the placement of the manipulator. In other words, the hyper-redundant manipulator cages the grasped object along the caging trace.

In order to guarantee the effectiveness of the caging and the operability of the hyper-redundant manipulator, the caging trace is discretized into a sequence of critical points connected by caging edges. These critical points are chosen as cross points between the caging curve and edges of the grasped object reasonably as shown in Fig. 4. Concretely, the discrete critical points are ordered. The first critical point, i.e., the caging origin, is denoted by $\boldsymbol{K}_1$, and the number of critical points is incremental along the caging direction until $\boldsymbol{K}_k$, k is the number of critical points. If the caging trace is closed, the tip of the hyper-redundant manipulator $\boldsymbol{E}$ coincides with $\boldsymbol{K}_1$; if the caging trace is open, $\boldsymbol{E}$ coincides with $\boldsymbol{K}_k$. To provide constraints, there must be joints of the hyper-redundant manipulator at each critical point. As mentioned in *Remark 1*, there is no need for a full match of the caging trace with the hyper-redundant manipulator because caging is a loose closure strategy with certain margin and allows changing the size of a caging configuration within the margin [13].

Remark 5: For the caged object whose natural edges are ambiguous, such as the cylinder and the circular cone, there are usually no natural segmentation points for a caging trace. At this point, the caging trace can be discretized according to the link number of the hyper-redundant manipulator. In addition, subject to the structural constraints, the hyper-redundant manipulator may not match with the given critical points perfectly. Alternatively, it forms an envelope around the caging trace (such as the circular trace shown in Fig. 7(a)).

Until now, the tracking of the caging trace by the hyper-redundant manipulator can be described as follows: a) given a caging trace with uncertainty and its corresponding caging origin/direction; b) find suitable joint angles of the hyper-redundant manipulator to realize the match of critical joints. The dynamic sequential caging following algorithm based on RRT algorithm is proposed and its flow chart is shown in Table 5.

3) DYNAMIC SEQUENTIAL CAGING FOLLOWING ALGORITHM BASED ON RRT ALGORITHM

As shown in Table 5, the inputs of the proposed algorithm are the joint angles limitation of the hyper-redundant manipulator $\theta_i \in [\theta_{il}, \theta_{iu}]$ and $\psi_i \in [\psi_{il}, \psi_{iu}](i = 1, 2, \cdots, n)$, the prototypical critical points set $\boldsymbol{K} = \{\boldsymbol{K}_1, \boldsymbol{K}_2, \ldots, \boldsymbol{K}_k\}$, the link length set of the hyper-redundant manipulator $L = \{l_1, l_2, \ldots, l_n\}$, and the preplanned matching joints group $J = \{J_{s1}, J_{s2}, \ldots, J_{sk}\}$. The outputs are the valid match sequence between $\boldsymbol{K} = \{\boldsymbol{K}_1, \boldsymbol{K}_2, \ldots, \boldsymbol{K}_k\}$ and $J = \{J_{s1}, J_{s2}, \ldots, J_{sk}\}$, and corresponding joint angles θ_i and ψ_i.

The principle to determine the matched sequence is to guarantee that the total link length between $J_{si} \sim J_{s(i+1)}$ happens to be no less than than the Euclidean distance of $\boldsymbol{K}_i \sim \boldsymbol{K}_{i+1}$ denoted by $\mathrm{Dist}(\boldsymbol{K}_i, \boldsymbol{K}_{i+1})$ as shown in (11).

$$\begin{cases} case1: s(i+1) - si = 1 \\ s.t. Dist(K_i, K_{i+1}) = l_{si} \\ case2: s(i+1) - si \geq 2: \\ s.t. \sum_{j=si}^{s(i+1)-2} l_j < Dist(K_i, K_{i+1}) \leq \sum_{j=si}^{s(i+1)-1} l_j \end{cases} \tag{11}$$

Remark 6: $\boldsymbol{K}$ and J are likely to change during the caging process due to the uncertainty of the caging trace. Therefore, the validity of the information of the critical points and matched sequence should be checked in real-time. For convenience, the matched sequence set $C = \{C_1, C_2, \ldots, C_{k-1}\}$ are calculated where $C_i = J_{s(i+1)} - J_{si}$. Consequently, C is also changing.

The dynamic sequential caging following algorithm based on RRT algorithm includes two main parts: matching the critical points sequentially and adjusting the matched critical points and joints locally. The aim of matching the critical points sequentially is to realize the match of $\boldsymbol{K}_i$ and J_{si} in turn as shown in Fig. 9. During the match of $\boldsymbol{K}_i$ and J_{si}, only joints $J_{s(i-1)} \sim J_{si-1}$ are searched by RRT algorithm and other joints remains their initial values, which will decrease the search dimension of RRT algorithm greatly. The concrete steps of RRT algorithm are shown in steps **20-34** in Table 5.

TABLE 5. The detail of the dynamic sequential caging following algorithm.

Inputs: $\theta_i \in [\theta_{il}, \theta_{iu}]$, $\psi_i \in [\psi_{il}, \psi_{iu}]$, k, $\boldsymbol{K} = \{\boldsymbol{K}_1, \boldsymbol{K}_2, \ldots, \boldsymbol{K}_k\}$, $L = \{l_1, l_2, \ldots, l_n\}$, $J = \{J_{s1}, J_{s2}, \ldots, J_{sk}\}$
Outputs: the valid match sequence between $\boldsymbol{K} = \{\boldsymbol{K}_1, \boldsymbol{K}_2, \ldots, \boldsymbol{K}_k\}$ and $J = \{J_{s1}, J_{s2}, \ldots, J_{sk}\}$, and corresponding joint angles θ_i and ψ_i

1: set $cur\_k = 1$, $\theta_{i0} = 0°$, $\psi_{i0} = 0°$; calculate the prototypical matched sequence set $C = \{C_1, C_2, \ldots, C_{k-1}\}$ where $C_i = J_{s(i+1)} - J_{si}$; match J_{s1} with $\boldsymbol{K}_1$
2: while $cur\_k < k$
3: **if** the preplanned matched sequence set $C = \{C_1, C_2, \ldots, C_{k-1}\}$ is valid
4: go to step **15**
5: **else**
6: update $\boldsymbol{K} = \{\boldsymbol{K}_1, \boldsymbol{K}_2, \ldots, \boldsymbol{K}_k\}$, update the matched sequence between $\boldsymbol{K}$ and $J = \{J_{s1}, J_{s2}, \ldots, J_{sk}\}$
7: recalculate the matched sequence set $C = \{C_1, C_2, \ldots, C_{k-1}\}$
8: **if** the match between $\boldsymbol{K}_1 \sim \boldsymbol{K}_{cur\_k}$ and $J_{s1} \sim J_{s(cur\_k)}$ is valid
9: go to step **15**
10: **else**
11: adjust $J_{s1} \sim J_{s(cur\_k)}$ locally to realize a valid match
12: go to step **15**
13: **end**
14: **end**
15: calculate the coordinate transformation matrix of $J_{s(cur\_k+1)}$ to get its position $\boldsymbol{p}_{s(cur\_k+1)}$
16: **if** $\left\|\boldsymbol{p}_{s(cur\_k+1)} - \boldsymbol{K}_{cur\_k+1}\right\| = 0$
17: $cur\_k = cur\_k + 1$
18: go to step **2**
19: **else**
20: initialize $\boldsymbol{q}_0$ with $J_{s(cur\_k)} \sim J_{s(cur\_k-1)}$ as the root node of RRT, set the number of seeds N_I and $cur_i = 1$
21: **if** $cur_i \leq N_I$
22: generate joint angle values of $J_{s(cur\_k)} \sim J_{s(cur\_k+1)} - 1$ within their limitation randomly as $\boldsymbol{q}_{rand} = rand(C(cur\_k), 1)$
23: select the node $\boldsymbol{q}_{near}$ in the RRT tree that is closest to $\boldsymbol{q}_{rand}$
24: generate a new node $\boldsymbol{q}_{new}$ between $\boldsymbol{q}_{near}$ and $\boldsymbol{q}_{rand}$
25: **if** there is no collision between $\boldsymbol{K}_{cur_k} \sim \boldsymbol{K}_{cur_k+1}$ and $J_{s(cur_k)} \sim J_{s(cur\_k+1)}$
26: $\boldsymbol{q}_{cand} = \boldsymbol{q}_{new}$
27: go to step **15**
28: **else**
29: $cur_i = cur_i + 1$
30: go to step **20**
31: **end**
32: **else**
33: go to step **20**
34: **end**
35: **end**
36: end

Specifically, the nearest node $\boldsymbol{q}_{near}$ in the current caging configuration path branches is selected by minimum norm calculation. The generation of new node $\boldsymbol{q}_{new}$ should satisfy the kinematics/dynamics constraints of the hyper-redundant manipulator as shown in (12). Here, *stepsize* is decided by the joint angle velocity/acceleration. In addition, each component of $\boldsymbol{q}_{new}$ should be within its own range.

$$\boldsymbol{q}_{new} = \boldsymbol{q}_{near} + stepsize \times (\boldsymbol{q}_{rand} - \boldsymbol{q}_{near}) \tag{12}$$

After obtaining $\boldsymbol{q}_{new}$, the collision detection is implemented to check its validity by the polygonal envelope detection algorithm [28]. In this paper, the caging trace is polygonal and the hyper-redundant manipulator is a chain structure. As shown in Fig. 10, there are no collision between the grasped object and the hyper-redundant manipulator when the distance d_j from the mass center of the grasped object to the jth($j = si \sim s(i+1) - 1$) link is no less than the distance d_i from the mass center of the grasped object to the caging edge $\boldsymbol{K}_i \sim \boldsymbol{K}_{i+1}$. Apparently, the collision detection of each caging edge is independent.

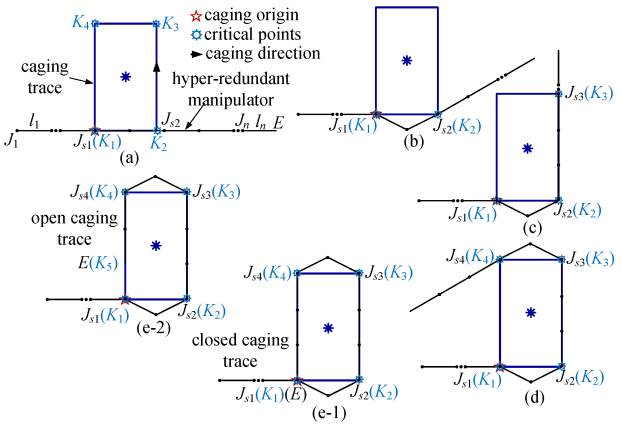

FIGURE 9. Illustration of the matching process.

Due to the uncertainty of the caging trace, the validity of the matched critical points $\boldsymbol{K}_1 \sim \boldsymbol{K}_{i-1}$ and joints $J_{s1} \sim J_{s(i-1)}$ is required to be tested before the match of $\boldsymbol{K}_i$ and J_{si}, which is the task of the adjusting the matched critical points and joints locally. Concrete uncertainty handling steps are shown in

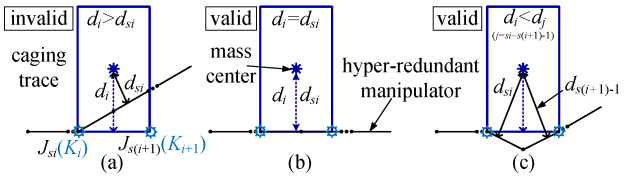

FIGURE 10. Illustration of the polygonal envelope detection algorithm (take the rectangular caging trace as an example).

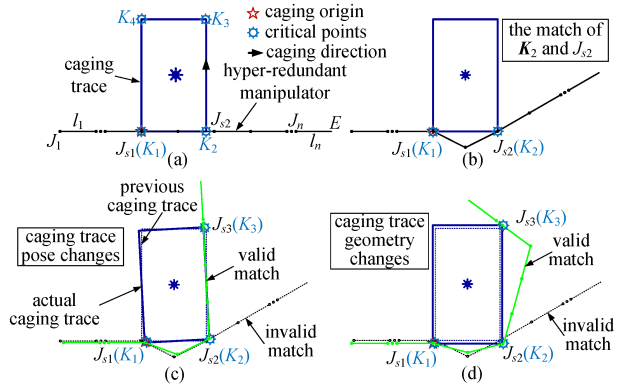

FIGURE 11. Illustration of adjusting the matched critical points and joints locally (take the rectangular caging trace as an example).

steps **3-14** in Table 5. As shown in Fig. 11, the pose or geometry of the caging trace may be changing, which results in the invalidity of the previous match. Concretely, the validity test includes the collision detection and the match detection. If the previous match is invalid, the values of $J_{s1} \sim J_{s(i-1)}$ are adjusted locally to towards a valid match. Likewise, RRT algorithm is adopted to search a valid match based on the previous values of $J_{s1} \sim J_{s(i-1)}$. Fortunately, the search range is limited within a small value $\triangle$ because the variation of the caging trace is limited. In addition, $\triangle$ is determined by the degree of uncertainty of the caging trace.

As described before, matching the critical points sequentially and adjusting the matched critical points and joints locally are crossed in the dynamic sequential caging following algorithm based on RRT algorithm. The main advantages of the proposed caging motion planning algorithm lie in the avoidance of inverse kinematics and the efficiency of computation.

IV. SIMULATIONS

The proposed algorithm has been implemented in MATLAB and some simulations have been carried out to prove its validity. The structure configuration of the simulation example is shown in Fig. 5. Further, assume each link of the hyper-redundant manipulator is same. The parameters of the hyper-reduandant are shown in Table 3. Other simulation parameters are shown in Table 6. Two representative satellites with different geometric shapes are chosen to verify the effectiveness of our method.

TABLE 6. Simulation parameters.

Parameters	Values
dysfunctional satellite 1	mainbody: regular hexagonal prism solar panels: unfilled triangle & filled rectangle mainbody size: side length a=0.4m and height h_h=1m solar panel size: length a_t=0.3m and a_r=1m, height h_s=0.6m
dysfunctional satellite 2	mainbody: cylinder solar panels: unfilled triangle & filled rectangle mainbody size: radius r=0.6m and height h_c=1m solar panel size: length a_t=0.5m and a_r=1.5m, height h_s=0.8m
initial conditions 1	${}^I\boldsymbol{T}_0$= [1 0 0 2;0 1 0 2;0 0 1 2;0 0 0 1] ${}^0\boldsymbol{T}_1$= [1 0 0 0;0 0 1 0.5;0 −1 0 0;0 0 0 1] ${}^{s1}\boldsymbol{T}_t$= [0 1 0 0;0 0 −1 0.5;−1 0 0 0.3464;0 0 0 1]
initial conditions 2	${}^I\boldsymbol{T}_0$= [1 0 0 1.3072;0 1 0 1.8;0 0 1 1.5;0 0 0 1] ${}^0\boldsymbol{T}_1$= [1 0 0 0;0 0 1 0.5;0 −1 0 0;0 0 0 1] ${}^{s1}\boldsymbol{T}_t$= [0 1 0 −0.2;0 0 −1 0;−1 0 0 −0.3464;0 0 0 1]
initial conditions 3	${}^I\boldsymbol{T}_0$= [1 0 0 2;0 1 0 2;0 0 1 2;0 0 0 1] ${}^0\boldsymbol{T}_1$= [1 0 0 0;0 0 1 0.5;0 −1 0 0;0 0 0 1] ${}^{s1}\boldsymbol{T}_t$= [1 0 0 −0.6392;0 1 0 0;0 1 0 −0.5;0 0 0 1]

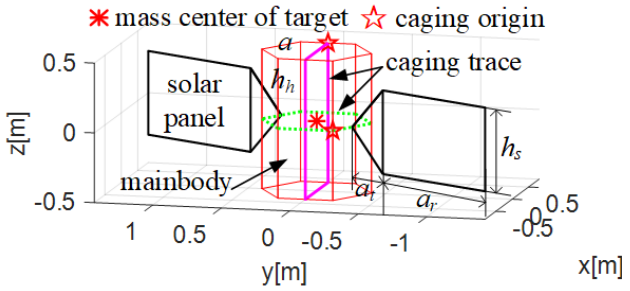

FIGURE 12. Several examples of the solutions of $\psi_3 \sim \psi_6$ and $\theta_3 \sim \theta_6$. (a) is random geometry. (b) is trigonal geometry.

A. CAGING A SATELLITE WITH A HEXAHEDRON MAINBODY

Fig. 12 shows the dysfunctional satellite 1 and the two caging traces. The caging trace denoted by pink solid lines dose not utilize the solar panels, while the caging trace denoted by green dotted lines utilizes the solar panels. In the following parts, we first show the strategy of the match of one caging edge; next, the match of a certain caging trace is implemented; then, the match of a caging trace with uncertainty is carried out; finally, the match considering solar panels is implemented.

Remark 7: For simplicity, the solar panels are ignored in the following simulation charts if the given caging trace dose not consider them. Initial conditions 1 and initial conditions 2 shown in Table 6 are set for the pink solid caging trace and green dotted caging trace, respectively.

1) THE STRATEGY OF ONE CAGING EDGE MATCH

Take the first caging edge of the pink caging trace as an example to illustrate the strategy. Assume J_3 matches with $\boldsymbol{K}_1$. For the first caging edge $\boldsymbol{K}_1 \sim \boldsymbol{K}_2$, its length satisfies $3l < Dist(K_1, K_2) = \sqrt{3}\,a < 4l$, thus 4 links are required to realize matching with $\boldsymbol{K}_2$. Apparently, to realize the match of the first edge is to find suitable values of $\psi_3 \sim \psi_6$ and $\theta_3 \sim \theta_6$ that makes J_7 matches with $\boldsymbol{K}_2$. Due to the randomness of RRT algorithm, the solutions of $\psi_3 \sim \psi_6$ and $\theta_3 \sim \theta_6$

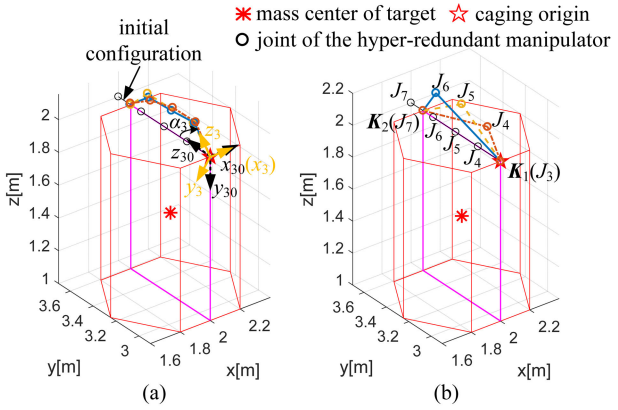

FIGURE 13. Several examples of the solutions of $\psi_3 \sim \psi_6$ and $\theta_3 \sim \theta_6$. (a) is random geometry. (b) is trigonal geometry.

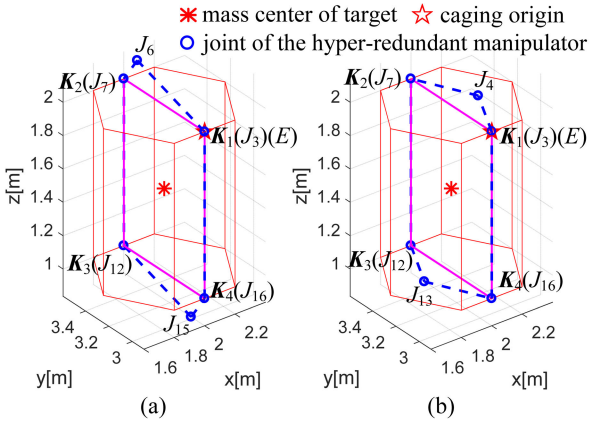

FIGURE 14. Solution of the match of the pink caging trace adopting the optimal trigonal geometry matching strategy where (a) and (b) are two different optimal trigonal geometries.

are usually not unique. Fig. 13 shows several examples of solutions. Apparently, only $\psi_3 \sim \psi_6$ are required to be adjusted to realize the match of J_7 and $\boldsymbol{K}_2$ from the initial configuration. Theoretically, the geometry composed by $\boldsymbol{K}_1$, $\boldsymbol{K}_2$ and $J_3 \sim J_7$ is various. As shown in Fig. 13, the trigonal geometry is the closest to $\boldsymbol{K}_1 \sim \boldsymbol{K}_2$. In addition, the number of actuated joints of the trigonal geometry strategy is reduced greatly, which will improve the calculation efficiency.

If $J_{s(i+1)}$ cannot match with $\boldsymbol{K}_{i+1}$ under the initial configuration, the trigonal geometry is adopted to reduce the complexity of RRT algorithm and make the caging configuration more stable. Then, the theoretical solution can be found. Specifically, for an arbitrary caging edge $\boldsymbol{K}_i \sim \boldsymbol{K}_{i+1}$, $J_{si} \sim J_{s(i+1)}$ must be coplanar with $\boldsymbol{K}_i \sim \boldsymbol{K}_{i+1}$. Thus, only ψ_{si} and $\theta_{si} \sim \theta_{s(i+1)-1}$ or θ_{si} and $\psi_{si} \sim \psi_{s(i+1)-1}$ are required to be adjusted where ψ_{si} or θ_{si} controls $J_{si} \sim J_n$ to be collinear with $\boldsymbol{K}_i \sim \boldsymbol{K}_{i+1}$, and $\psi_{si} \sim \psi_{s(i+1)-1}$ or $\theta_{si} \sim \theta_{s(i+1)-1}$ makes $J_{s(i+1)}$ to match with $\boldsymbol{K}_{i+1}$. Since J_{si} has matched with $\boldsymbol{K}_i$, we divide $J_{si} \sim J_{s(i+1)}$ into two groups: $J_{si} \sim J_{mi}$ and $J_{mi} \sim J_{s(i+1)}$. The links between J_{si} and J_{mi} work as an integral link denoted by L_{sim}, and the links between J_{mi} and $J_{s(i+1)}$ also work as an integral link denoted by $L_{ms(i+1)}$. The principle to determine the middle node is to guarantee that the length of L_{sim} denoted by l_{sim}, the length of $L_{ms(i+1)}$ denoted by $l_{ms(i+1)}$ and the length of caging edge $\boldsymbol{K}_i \sim \boldsymbol{K}_{i+1}$ denoted by $l_{i(i+1)}$ satisfy the constructive condition of triangle, i.e., the sum of any two sides of a triangle is greater than the third side and the difference of any two sides of a triangle is less than the third side. According to the cosine law, the angle between L_{sim} and $\boldsymbol{K}_i \sim \boldsymbol{K}_{i+1}$ denoted by γ_{i1}, and the angle between L_{sim} and $l_{ms(i+1)}$ denoted by γ_{i2} are as shown in (13) and (14), respectively. The signs and concrete values of J_{si} and J_{mi} are determined by the rotation direction. For example, for the blue solid trigonal geometry shown in Fig. 13(b),$J_{mi} = J_6$, $\theta_{si} = 0°$, $\psi_{si} = \gamma_{i1} = 15.79°$ and $\psi_{mi} = -(180° - \gamma_{i2}) = -70.53°$. In addition, the blue solid and brown dotted trigonal geometries whose one side is one link of the hyper-redundant manipulator are closest to $\boldsymbol{K}_1 \sim \boldsymbol{K}_2$ among all the trigonal geometries, and this kind trigonal geometry will be chosen preferentially in the following simulations.

$$\gamma_{i1} = \frac{l_{sim}^2 + l_{i(i+1)}^2 - l_{ms(i+1)}^2}{2 l_{sim} l_{i(i+1)}} \tag{13}$$

$$\gamma_{i2} = \frac{l_{sim}^2 + l_{ms(i+1)}^2 - l_{i(i+1)}^2}{2 l_{sim} l_{ms(i+1)}} \tag{14}$$

2) THE CERTAIN CAGING TRACE MATCH

If the pink caging trace is certain, the solutions of the match by the hyper-redundant manipulator adopting the optimal trigonal geometry matching strategy are shown in Fig. 14. Assume simulation conditions are the same as those in subsection IV-A.1. Take the first optimal trigonal geometry shown in Fig. 14(a) as an example to illustrate the match in detail. Assume J_3 matches with $\boldsymbol{K}_1$, i.e., $J_{s1} = J_3$. The results are shown in Table 7. Then, for the first caging edge $\boldsymbol{K}_1 \sim \boldsymbol{K}_2$, its length satisfies $3l < Dist(K_1, K_2) = \sqrt{3}\, a < 4l$, thus 4 links are required to realize matching with $\boldsymbol{K}_2$. For the second caging edge $\boldsymbol{K}_2 \sim \boldsymbol{K}_3$, its length is just equal to $5l$, thus 5 links are required to realize matching with $\boldsymbol{K}_3$. For the third caging edge $\boldsymbol{K}_3 \sim \boldsymbol{K}_4$, its length satisfies $3l < Dist(K_3, K_4) = \sqrt{3}\, a < 4l$, thus 4 links are required to realize matching with $\boldsymbol{K}_4$. For the fourth caging edge $\boldsymbol{K}_4 \sim \boldsymbol{K}_5$, its length is just equal to $5l$, thus 5 links are required to realize matching with $\boldsymbol{K}_5$. The solution procedure of the second optimal trigonal geometry shown in Fig. 14(b) is similar to the first optimal trigonal geometry. Therefore, for the these solutions, J_3 matches with $\boldsymbol{K}_1$, J_7 matches with $\boldsymbol{K}_2$, J_{12} matches with $\boldsymbol{K}_3$, J_{16} matches with $\boldsymbol{K}_4$ and $\boldsymbol{E}$ coincides with $\boldsymbol{K}_5$. Finally, the matched sequence set between $\boldsymbol{K} = \{\boldsymbol{K}_1, \boldsymbol{K}_2, \boldsymbol{K}_3, \boldsymbol{K}_4, \boldsymbol{K}_5\}$ and joints $J = \{J_3, J_7, J_{12}, J_{16}, E\}$ is $C = \{4, 5, 4, 5\}$.

3) THE MATCH OF A CAGING TRACE WITH UNCERTAINTY

The former two simulations illustrate the strategy of matching with a certain caging trace. However, for the dysfunctional satellite with uncertainty, its caging traces are usually uncertain to some degree, which means that the critical points are

TABLE 7. The results of certain caging trace match (first optimal trigonal geometry).

Caging edge	Match sequence	Joint angle values
$\boldsymbol{K}_1 \sim \boldsymbol{K}_2$	$J_{s1}(J_3) \to \boldsymbol{K}_1, J_{m1} \to J_6, J_{s2}(J_7) \to \boldsymbol{K}_2$	$\theta_{s1} = 0°, \psi_{s1} = \gamma_{11} = 15.79°, \psi_{m1} = -(180° - \gamma_{12}) = -70.53°$
$\boldsymbol{K}_2 \sim \boldsymbol{K}_3$	$J_{s2}(J_7) \to \boldsymbol{K}_2, J_{s3}(J_{12}) \to \boldsymbol{K}_3$	$\theta_{s2} = 0°, \psi_{s2} = -35.26°$
$\boldsymbol{K}_3 \sim \boldsymbol{K}_4$	$J_{s3}(J_{12}) \to \boldsymbol{K}_3, J_{m3} \to J_{15}, J_{s4}(J_{16}) \to \boldsymbol{K}_4$	$\theta_{s3} = 0°, \psi_{s3} = -(90°/2 - \gamma_{31}) = -74.21°, \psi_{m3} = -(180° - \gamma_{32}) = -70.53°$
$\boldsymbol{K}_4 \sim \boldsymbol{K}_5$	$J_{s4}(J_{16}) \to \boldsymbol{K}_4, \boldsymbol{E} \to \boldsymbol{K}_5$	$\theta_{s4} = 0°, \psi_{s4} = -35.26°$

time-varying. For the caging trace with uncertainty, the optimal trigonal geometry matching strategy is still adopted to find the theoretical goal solutions and RRT algorithm is utilized to search for a feasible path without collision from the initial geometry to the goal geometry in real-time.

As the caging process progresses, the measured information of grasped object will become more and more close to the actual information. For the pink caging trace, assume its actual geometry is larger than the measured prototypical one and there is a small relative angular velocity between the grasped object and the hyper-redundant manipulator. As a result, positions of the critical points will change. Assume the threshold of the uncertainty is $\triangle = 0.1$, that is to say, the caging trace is no more than the amplified 1.1 times of its initial measured values during the caging process. The random strategy is further adopted to simulate the change of the caging trace in real-time. Further, we assume that J_{s1} matches with $\boldsymbol{K}_1$ all the time no matter how $\boldsymbol{K}_1$ changes because this match maintainance of J_{s1} and $\boldsymbol{K}_1$ is done by the maneuver of the servicing satellite. It should be pointed out that the sequence rule is throughout the whole caging process, that is to say, the rotation of actuated joints is one by one.

The parameters of the grasped object is measured again when the match of $\boldsymbol{K}_2$ is going to be implemented. Unfortunately, the measured information of the grasped object is changed where its side length becomes 0.42m and its height becomes 1.06m, which causes the caging trace changes. As a result, the prototypical matched sequence between $\boldsymbol{K}$ and joints J may be improper. We will discuss the suboptimal caging situation and ideal caging situation in the following simulations, respectively.

Case 1: The suboptimal caging situation

If $J_{s1} = J_3$ remains unchanged, the matched sequence set will be $C = \{4, 6, 4, 4\}$ according to (11), which will correspond to the suboptimal situation (open caging trace). Fig. 15 shows the snapshots of the caging process of this suboptimal situation adopting the first optimal trigonal geometry where the black dotted lines and red solid lines represent the prototypical and updated measured information, respectively. The corredonding joint angles are shown in Table 8. Firstly, the first caging edge $\boldsymbol{K}_1 \sim \boldsymbol{K}_2$ is mathced, and Fig. 15(a) shows the result. Next, the second caging edge $\boldsymbol{K}_2 \sim \boldsymbol{K}_3$ is matched. The caging trace pose changes due to the attitude asynchronism (rotating $-5°$ around the z axis of the fixed coordinate system of the grasped object). To begin with, the validity of matched sequence set is checked, i.e., the validity matched critical points $\boldsymbol{K}_1 \sim \boldsymbol{K}_2$ and joints $J_{s1} \sim J_{s2}$ is tested. Fortunately, C is still effective and adjust the

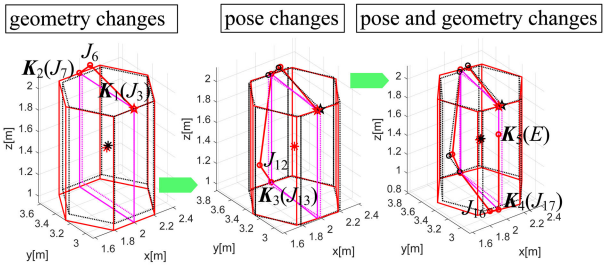

(a) match J_7 with $\boldsymbol{K}_2$ (b) match J_{13} with $\boldsymbol{K}_3$ (c) match J_{17} with $\boldsymbol{K}_4$

FIGURE 15. Snapshots of the caging process of the match of the pink caging trace with uncertainty (suboptimal situation).

matched critical points and joints locally can satisfy the validity requirement. Fig. 15(b) shows the results of match J_{s3} with $\boldsymbol{K}_3$. Then, the third caging edge $\boldsymbol{K}_3 \sim \boldsymbol{K}_4$ is matched. Similarly, the information of the grasped object is updated first, but it is unfortunate that both the geometry and pose of the grasped object change. Specifically, the side length a becomes 0.44m, the height h becomes 1.1m, and the grasped object rotates $-5°$ around the z axis of its fixed coordinate system. Through validity test, C is still effective, but the matched critical points $\boldsymbol{K}_1 \sim \boldsymbol{K}_3$ and joints $J_{s1} \sim J_{s3}$ are invalid. Fig. 15(c) shows the results of match J_{s4} with $\boldsymbol{K}_4$. Luckily, the caging trace doesn't change when $\boldsymbol{E}$ matches with $\boldsymbol{K}_5$ which means that the previous match is valid. In this suboptimal situation, $J_{s4} \sim \boldsymbol{E}$ should coincide with $\boldsymbol{K}_4 \sim \boldsymbol{K}_5$ to guarantee the opening length L_o=0.3m is less than L_c=1.1m. Fig. 15(c) shows the results of match $\boldsymbol{E}$ with $\boldsymbol{K}_5$.

Fig. 17 shows one valid searching path of actuated joints during the caging process, which corresponds to the sequence rule that the rotation of the actuated joints is one by one. More specifically, when implementing the match of the first caging edge $\boldsymbol{K}_1 \sim \boldsymbol{K}_2$, only θ_{s1}, ψ_{s1} and ψ_{m1} change, and other actuated joints keep their initial values. Further, the driving sequence is $\theta_{s1} \to \psi_{s1} \to \psi_{m1}$. For the match of the first caging edge $\boldsymbol{K}_2 \sim \boldsymbol{K}_3$, θ_{s1}, ψ_{s1} and ψ_{m1} are checked and adjusted first; then, θ_{s2}, ψ_{s2} and ψ_{m2} are searched. The same rules for the following match. In addition, Fig. 16 also illustrates that the joint motion is continuous.

Case 2: The ideal caging situation

To form a closed caging trace, the matched sequence set between $\boldsymbol{K}$ and joints J should be adjusted from its prototypical value $C = \{4, 5, 4, 5\}$ to an updated value $C = \{4, 6, 4, 6\}$. For this case, $J_{s1} = J_1$. Assume the change of the caging trace in the ideal caging situation is in the same mannar as that in the suboptimal caging situation. Fig. 17 shows

TABLE 8. The results of a caging trace match with uncertainty (the suboptimal caging situation).

Caging situation	Caging edge	Match sequence	Joint angle values
$\boldsymbol{K}_1 \sim \boldsymbol{K}_2$ match	$\boldsymbol{K}_1 \sim \boldsymbol{K}_2$	$J_{s1}(J_3) \to \boldsymbol{K}_1, J_{m1} \to J_6, J_{s2}(J_7) \to \boldsymbol{K}_2$	$\theta_{s1}^1 = 0°, \psi_{s1}^1 = 13.40°, \psi_{m1}^1 = -57.43°$
$\boldsymbol{K}_2 \sim \boldsymbol{K}_3$ match	$\boldsymbol{K}_1 \sim \boldsymbol{K}_2$	$J_{s1}(J_3) \to \boldsymbol{K}_1, J_{m1} \to J_6, J_{s2}(J_7) \to \boldsymbol{K}_2$	$\theta_{s1}^2 = 5°, \psi_{s1}^2 = 13.40°, \psi_{m1}^2 = -57.43°$
(pose change)	$\boldsymbol{K}_2 \sim \boldsymbol{K}_3$	$J_{s2}(J_7) \to \boldsymbol{K}_2, J_{m2} \to J_{12}, J_{s3}(J_{13}) \to \boldsymbol{K}_3$	$\theta_{s2}^2 = 0°, \psi_{s2}^2 = -35.33°, \psi_{m2}^2 = -77.94°$
$\boldsymbol{K}_3 \sim \boldsymbol{K}_4$ match	$\boldsymbol{K}_1 \sim \boldsymbol{K}_2$	$J_{s1}(J_3) \to \boldsymbol{K}_1, J_{m1} \to J_6, J_{s2}(J_7) \to \boldsymbol{K}_2$	$\theta_{s1}^3 = 10°, \psi_{s1}^3 = 9.94°, \psi_{m1}^2 = -41.12°$
(pose and geometry	$\boldsymbol{K}_2 \sim \boldsymbol{K}_3$	$J_{s2}(J_7) \to \boldsymbol{K}_2, J_{m2} \to J_{12}, J_{s3}(J_{13}) \to \boldsymbol{K}_3$	$\theta_{s2}^3 = 0°, \psi_{s2}^3 = -49.35°, \psi_{m2}^3 = -64.85°$
change)	$\boldsymbol{K}_3 \sim \boldsymbol{K}_4$	$J_{s3}(J_{13}) \to \boldsymbol{K}_3, J_{m3} \to J_{16}, J_{s4}(J_{17}) \to \boldsymbol{K}_4$	$\theta_{s3}^3 = 0°, \psi_{s3}^3 = -24.64°, \psi_{m3}^3 = -41.12°$
$\boldsymbol{K}_4 \sim \boldsymbol{K}_5(\boldsymbol{E})$ match	$\boldsymbol{K}_1 \sim \boldsymbol{K}_2$	$J_{s1}(J_3) \to \boldsymbol{K}_1, J_{m1} \to J_6, J_{s2}(J_7) \to \boldsymbol{K}_2$	$\theta_{s1}^4 = 10°, \psi_{s1}^4 = 9.94°, \psi_{m1}^4 = -41.12°$
	$\boldsymbol{K}_2 \sim \boldsymbol{K}_3$	$J_{s2}(J_7) \to \boldsymbol{K}_2, J_{m2} \to J_{12}, J_{s3}(J_{13}) \to \boldsymbol{K}_3$	$\theta_{s2}^4 = 0°, \psi_{s2}^4 = -49.35°, \psi_{m2}^4 = -64.85°$
	$\boldsymbol{K}_3 \sim \boldsymbol{K}_4$	$J_{s3}(J_{13}) \to \boldsymbol{K}_3, J_{m3} \to J_{16}, J_{s4}(J_{17}) \to \boldsymbol{K}_4$	$\theta_{s3}^4 = 0°, \psi_{s3}^4 = -24.64°, \psi_{m3}^4 = -41.12°$
	$\boldsymbol{K}_4 \sim \boldsymbol{K}_5(\boldsymbol{E})$	$J_{s4}(J_{17}) \to \boldsymbol{K}_4, \boldsymbol{E} \to \boldsymbol{K}_5$	$\theta_{s4}^4 = 0°, \psi_{s4}^4 = -58.81°, \psi_{m4}^4 = 0°$

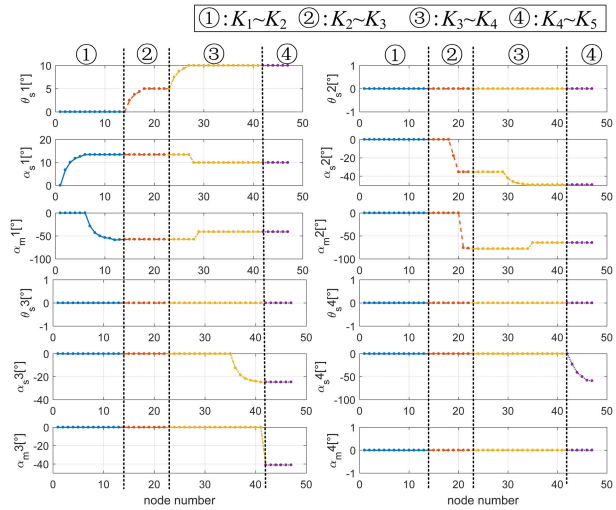

FIGURE 16. Path of the actuated joints during the caging process (suboptimal situation).

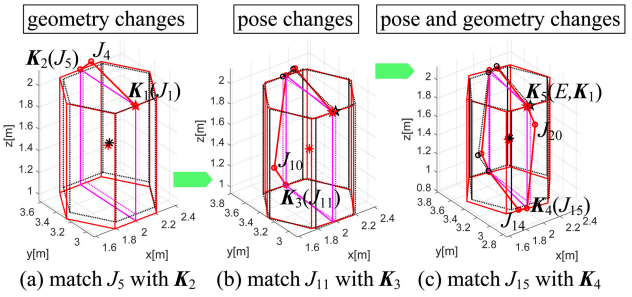

(a) match J_5 with $\boldsymbol{K}_2$ (b) match J_{11} with $\boldsymbol{K}_3$ (c) match J_{15} with $\boldsymbol{K}_4$

FIGURE 17. Snapshots of the caging process of the match of the pink caging trace with uncertainty (ideal situation).

the snapshots of the caging process adopting the first optimal trigonal geometry where the black dotted lines and red solid lines also represent the prototypical and updated measured information, respectively. Furthermore, Table 9 shows the corredonding joint angles. Similar to the suboptimal case, the caging edges match are sequential. It should be pointed out that $\boldsymbol{K}_5$ coincides with $\boldsymbol{K}_1$, thus the end point of the hyper-redundant manipulator $\boldsymbol{E}$ coincides with $\boldsymbol{K}_5$ and $\boldsymbol{K}_1$ simultaneously.

Fig. 18 shows one valid searching path of the actuated joints during the caging process, which is also continuous and corresponds to the sequence rule. For the suboptimal caging

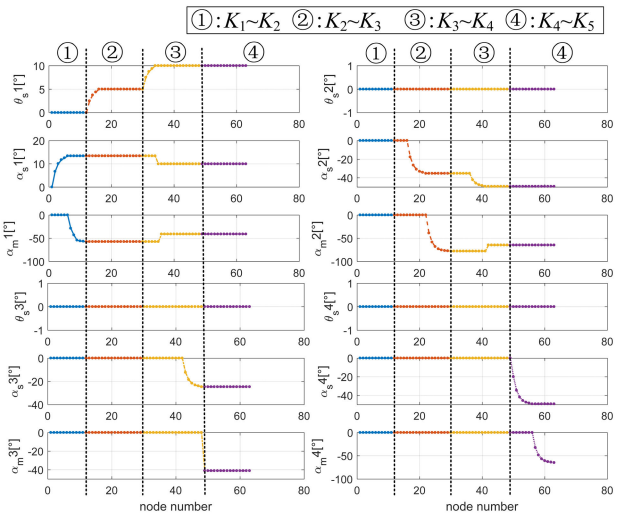

FIGURE 18. Path of the actuated joints during the caging process (ideal situation).

situation and the ideal situation, Fig. 16 and Fig. 18 show that there is difference of their joint paths though the values of actuated joints $J_{s1} \sim J_{m3}$ are same. In other words, the valid searching paths are various in theory.

4) THE MATCH OF A CAGING TRACE CONSIDERING SOLAR PANELS

Assume the hyper-redundant manipulator breaks down and only the links marked by 12 to 20 could work normally, which implies that only 9 links can be used to execute the caging operation. In this case, the critical points cannot be traversed, and the valid caging configuration cannot be achieved without the help of solar panels. J_{12} should match with $\boldsymbol{K}_1$, i.e., $J_{s1} = J_{12}$. The matched sequence set will be $C = \{2, 2, 2, 2, 1\}$ according to (11). It should be pointed out that, in this part, we only focus on the role of solar panels, and we ignore the uncertainty of the caging trace. Fig. 19 shows the snapshots of the caging process, and the corresponding joint angles are shown in Table 10. Limited by the links of hyper-redundant manipulator, only $\boldsymbol{K}_1 \sim \boldsymbol{K}_5$ and a part of $\boldsymbol{K}_5 \sim \boldsymbol{K}_6$ are matched. Fortunately, the existence of solar panels provides extra constraints, and the dysfunctional satellite can be caged. When the match of $\boldsymbol{K}_3 \sim \boldsymbol{K}_4$ is implemented, the hyper-redundant manipulator collides with the solar panel of the dysfunctional satellite. Thus, the angles of J_{s4} must be

TABLE 9. The results of a caging trace match with uncertainty (the ideal caging situation).

Caging situation	Caging edge	Match sequence	Joint angle values
$\boldsymbol{K}_1 \sim \boldsymbol{K}_2$ match	$\boldsymbol{K}_1 \sim \boldsymbol{K}_2$	$J_{s1}(J_1) \to \boldsymbol{K}_1, J_{m1} \to J_4, J_{s2}(J_5) \to \boldsymbol{K}_2$	$\theta_{s1}^1 = 0°, \psi_{s1}^1 = 13.40°, \psi_{m1}^1 = -57.43°$
$\boldsymbol{K}_2 \sim \boldsymbol{K}_3$ match	$\boldsymbol{K}_1 \sim \boldsymbol{K}_2$	$J_{s1}(J_1) \to \boldsymbol{K}_1, J_{m1} \to J_4, J_{s2}(J_5) \to \boldsymbol{K}_2$	$\theta_{s1}^2 = 5°, \psi_{s1}^2 = 13.40°, \psi_{m1}^2 = -57.43°$
(pose change)	$\boldsymbol{K}_2 \sim \boldsymbol{K}_3$	$J_{s2}(J_5) \to \boldsymbol{K}_2, J_{m2} \to J_{10}, J_{s3}(J_{11}) \to \boldsymbol{K}_3$	$\theta_{s2}^2 = 0°, \psi_{s2}^2 = -35.33°, \psi_{m2}^2 = -77.94°$
$\boldsymbol{K}_3 \sim \boldsymbol{K}_4$ match	$\boldsymbol{K}_1 \sim \boldsymbol{K}_2$	$J_{s1}(J_1) \to \boldsymbol{K}_1, J_{m1} \to J_4, J_{s2}(J_5) \to \boldsymbol{K}_2$	$\theta_{s1}^3 = 10°, \psi_{s1}^3 = 9.94°, \psi_{m1}^2 = -41.12°$
(pose and geometry	$\boldsymbol{K}_2 \sim \boldsymbol{K}_3$	$J_{s2}(J_5) \to \boldsymbol{K}_2, J_{m2} \to J_{10}, J_{s3}(J_{11}) \to \boldsymbol{K}_3$	$\theta_{s2}^3 = 0°, \psi_{s2}^3 = -49.35°, \psi_{m2}^3 = -64.85°$
change)	$\boldsymbol{K}_3 \sim \boldsymbol{K}_4$	$J_{s3}(J_{11}) \to \boldsymbol{K}_3, J_{m3} \to J_{14}, J_{s4}(J_{15}) \to \boldsymbol{K}_4$	$\theta_{s3}^3 = 0°, \psi_{s3}^3 = -24.64°, \psi_{m3}^3 = -41.12°$
$\boldsymbol{K}_4 \sim \boldsymbol{K}_5(\boldsymbol{E})$ match	$\boldsymbol{K}_1 \sim \boldsymbol{K}_2$	$J_{s1}(J_1) \to \boldsymbol{K}_1, J_{m1} \to J_4, J_{s2}(J_5) \to \boldsymbol{K}_2$	$\theta_{s1}^4 = 10°, \psi_{s1}^4 = 9.94°, \psi_{m1}^4 = -41.12°$
	$\boldsymbol{K}_2 \sim \boldsymbol{K}_3$	$J_{s2}(J_5) \to \boldsymbol{K}_2, J_{m2} \to J_{10}, J_{s3}(J_{11}) \to \boldsymbol{K}_3$	$\theta_{s2}^4 = 0°, \psi_{s2}^4 = -49.35°, \psi_{m2}^4 = -64.85°$
	$\boldsymbol{K}_3 \sim \boldsymbol{K}_4$	$J_{s3}(J_{11}) \to \boldsymbol{K}_3, J_{m3} \to J_{14}, J_{s4}(J_{15}) \to \boldsymbol{K}_4$	$\theta_{s3}^4 = 0°, \psi_{s3}^4 = -24.64°, \psi_{m3}^4 = -41.12°$
	$\boldsymbol{K}_4 \sim \boldsymbol{K}_5(\boldsymbol{E})$	$J_{s4}(J_{15}) \to \boldsymbol{K}_4, J_{m4} \to J_{20}, \boldsymbol{E} \to \boldsymbol{K}_5(\boldsymbol{K}_1)$	$\theta_{s4}^4 = 0°, \psi_{s4}^4 = -49.35°, \psi_{m4}^4 = -64.85°$

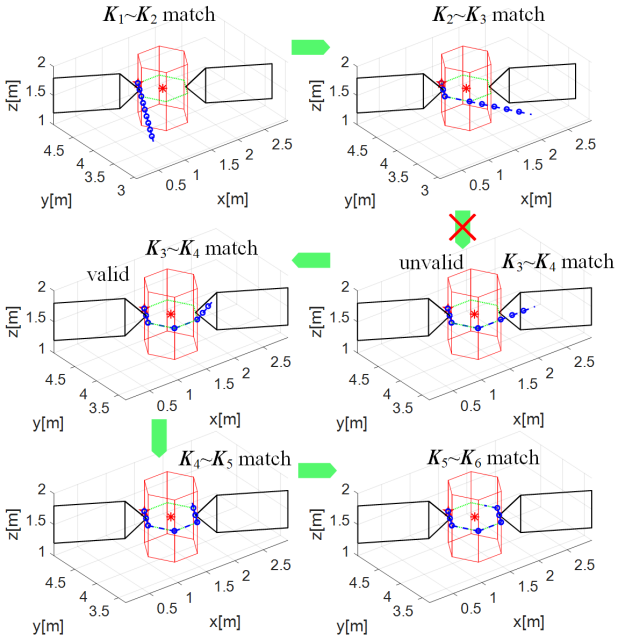

FIGURE 19. Snapshots of the caging process of the match of the caging trace considering solar panels.

TABLE 10. The results of caging trace match considering solar panels.

Caging edge	Match sequence	Joint angle values
$\boldsymbol{K}_1 \sim \boldsymbol{K}_2$	$J_{s1}(J_{12}) \to \boldsymbol{K}_1, J_{s2}(J_{14}) \to \boldsymbol{K}_2$	$\theta_{s1} = -150°, \psi_{s1} = 0°$
$\boldsymbol{K}_2 \sim \boldsymbol{K}_3$	$J_{s2}(J_{14}) \to \boldsymbol{K}_2, J_{s3}(J_{16}) \to \boldsymbol{K}_3$	$\theta_{s2} = -60°, \psi_{s2} = 0°$
$\boldsymbol{K}_3 \sim \boldsymbol{K}_4$	$J_{s3}(J_{16}) \to \boldsymbol{K}_3, J_{s4}(J_{18}) \to \boldsymbol{K}_4$	$\theta_{s3} = -60°, \psi_{s3} = 0°$
$\boldsymbol{K}_4 \sim \boldsymbol{K}_5$	$J_{s4}(J_{18}) \to \boldsymbol{K}_4, J_{s5}(J_{20}) \to \boldsymbol{K}_5$	$\theta_{s4} = -60°, \psi_{s4} = 0°$
$\boldsymbol{K}_5 \sim \boldsymbol{K}_6$	$J_{s5}(J_{20}) \to \boldsymbol{K}_5, J_{s6} \neq \boldsymbol{E}$	$\theta_{s5} = -60°, \psi_{s5} = 0°$

adjusted during this operation to ensure safety. In this case, the transition values are $\theta_{s4} = -30°$ and $\psi_{s4} = 0°$.

B. CAGING A SATELLITE WITH A CYLINDER MAINBODY

In this part, the dysfunctional satellite 2 with a cylinder mainbody is caged, of which the caging trace is a circle without natural separation. Initial conditions 3 shown in Table 6 are adopted. The chosen caging trace also goes through the solar panels. To match with the given caging trace as close as possible, each link of the hyper-redundant manipulator is

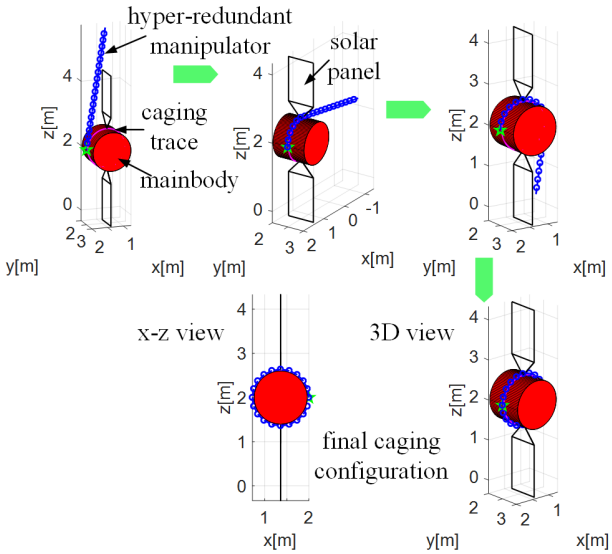

FIGURE 20. Snapshots of the caging process of the match of the circular caging trace.

actuated separately. Fig. 20 shows the snapshots of the caging process.

V. CONCLUSION

An adaptive caging configuration design algorithm of hyper-redundant manipulator for dysfunctional satellite pre-capture is presented in this paper. Through the demonstration of theoretical analysis and simulation, the main conclusions are as follows:

(1) The hyper-redundant manipulator can use its whole body to wrap around the grasped object to restrain its motion without needing grappling points and accurate inforamtion.

(2) The derived caging conditions of the hyper-redundant manipulator through static analysis and dynamic analysis are used directly for judging whether an effective caging configuraiton is achieved or not.

(3) The proposed dynamic sequential caging following algorithm based on RRT algorithm can search the caging configuration in real-time, which can avoid the inverse kinematics and improve computational efficiency.

(4) Through the simulation examples, we find that the trigonal geometry is closest to the caging edge and can reduce

the number of actuated joints, so it is adopted as the match strategy for the caging trace composed of line segments. In addition, the solar panels play an important role to offer additional constraints.

In future work, we will study how to grasp and manipulate a dysfunctional satellite, and the real experiments must be conducted to verify whether our method is practical and valid.

ACKNOWLEDGMENT

The authors would like to thank the editors and reviewers for their careful reading, comments and suggestions on improving the manuscript.

REFERENCES

[1] M. Shan, J. Guo, and E. Gill, "Review and comparison of active space debris capturing and removal methods," *Progr. Aerosp. Sci.*, vol. 80, pp. 18–32, Jan. 2016.
[2] D. Reintsema, J. Thaeter, A. Rathke, W. Naumann, P. Rank, and J. Sommer, "Deos—The German robotics approach to secure and de-orbit malfunctioned satellites from low earth orbits," in *Proc. Int. Symp. Artif. Intell. Robot. Autom. Space*, Sapporo, Japan, Aug./Sep. 2010, pp. 244–251.
[3] B. Bischof, "Roger–robotic geostationary orbit restorer," in *Proc. 54th Int. Astron. Congr. Int. Astron. Fed., Int. Acad. Astronaut., Int. Inst. Space Law*, Bremen, Germany, Sep./Oct. 2003, p. IAA-5.
[4] J. L. Forshaw, G. S. Aglietti, N. Navarathinam, H. Kadhem, T. Salmon, A. Pisseloup, E. Joffre, T. Chabot, I. Retat, R. Axthelm, S. Barraclough, A. Ratcliffe, C. Bernal, F. Chaumette, A. Pollini, and W. H. Steyn, "RemoveDEBRIS: An in-orbit active debris removal demonstration mission," *Acta Astronautica*, vol. 127, pp. 448–463, Oct. 2016.
[5] B. Liang, X. D. Du, C. Li, and W. F. Xu, "Advances in space robot on-orbit servicing for non—Cooperative spacecraft," *Robot*, vol. 34, pp. 242–256, Mar. 2012.
[6] A. Flores-Abad, O. Ma, K. Pham, and S. Ulrich, "A review of space robotics technologies for on-orbit servicing," *Progr. Aerosp. Sci.*, vol. 68, pp. 1–26, Jul. 2014.
[7] M. Chu and X. Wu, "Modeling and self-learning soft-grasp control for free-floating space manipulator during target capturing using variable stiffness method," *IEEE Access*, vol. 6, pp. 7044–7054, 2018.
[8] G. Chirikjian and J. Burdick, "Kinematics of hyper-redundant robot locomotion with applications to grasping," in *Proc. IEEE Int. Conf. Robot. Autom.*, Sacramento, CA, USA, Dec./Apr. 2002, pp. 720–725.
[9] W. Xu, Z. Mu, T. Liu, and B. Liang, "A modified modal method for solving the mission-oriented inverse kinematics of hyper-redundant space manipulators for on-orbit servicing," *Acta Astronautica*, vol. 139, pp. 54–66, Oct. 2017.
[10] G. Chirikjian and J. Burdick, "A modal approach to hyper-redundant manipulator kinematics," *IEEE Trans. Robot. Automat.*, vol. 10, no. 3, pp. 343–354, Jun. 1994.
[11] M. W. Hannan and I. D. Walker, "Kinematics and the implementation of an elephant's trunk manipulator and other continuum style robots," *J. Robot. Syst.*, vol. 20, no. 2, pp. 45–63, Jul. 2010.
[12] E. Rimon and A. Blake, "Caging 2D bodies by 1-parameter two-fingered gripping systems," in *Proc. IEEE Int. Conf. Robot. Autom.*, Minneapolis, MN, USA, Dec. 2002, pp. 1458–1464.
[13] Z. Wang, Y. Hirata, and K. Kosuge, "Control a rigid caging formation for cooperative object transportation by multiple mobile robots," in *Proc. IEEE Int. Conf. Robot. Autom. (ICRA)*, New Orleans, LA, USA, Apr. 2004, pp. 1580–1585.
[14] S. Makita and W. Wan, "A survey of robotic caging and its applications," *Adv. Robot.*, vol. 31, nos. 19–20, pp. 1071–1085, Oct. 2017.
[15] G. Wang, Z. Xie, Y. Lu, J. Wang, M. Wu, F. Yang, H. Yue, and S. Jiang, "Analysis method of the capture tolerance capability for an orthogonally distributed satellite capture device," *IEEE Access*, vol. 7, pp. 55022–55034, 2019.
[16] G. Chirikjian, "A continuum approach to hyper-redundant manipulator dynamics," in *Proc. IEEE/RSJ Int. Conf. Intell. Robots Syst. (IROS)*, Yokohama, Japan, Dec. 2002, pp. 1059–1066.
[17] H. Mohamed, S. Yahya, M. Moghavvemi, and S. Yang, "A new inverse kinematics method for three dimensional redundant manipulators," in *Proc. ICCAS-SICE*, Fukuoka, Japan, Aug. 2009, pp. 1557–1562.
[18] Z. Mu, H. Yuan, W. Xu, T. Liu, and B. Liang, "A segmented geometry method for kinematics and configuration planning of spatial hyper-redundant manipulators," *IEEE Trans. Syst., Man, Cybern. Syst.*, to be published.
[19] A. Colome and C. Torras, "Closed-loop inverse kinematics for redundant robots: Comparative assessment and two enhancements," *IEEE/ASME Trans. Mechatronics*, vol. 20, no. 2, pp. 944–955, Apr. 2015.
[20] W. Xu, J. Zhang, B. Liang, and B. Li, "Singularity analysis and avoidance for robot manipulators with nonspherical wrists," *IEEE Trans. Ind. Electron.*, vol. 63, no. 1, pp. 277–290, Jan. 2016.
[21] C. Y. Sun, W. He, W. L. Ge, and C. Chang, "Adaptive neural network control of biped robots," *IEEE Trans. Syst., Man, Cybern. Syst.*, vol. 47, no. 2, pp. 315–326, Feb. 2017.
[22] M. Wang and A. Yang, "Dynamic learning from adaptive neural control of robot manipulators with prescribed performance," *IEEE Trans. Syst. Man Cybern, Syst.*, vol. 47, no. 8, pp. 2244–2255, Aug. 2017.
[23] S. Li, Y. Zhang, and L. Jin, "Kinematic Control of Redundant Manipulators Using Neural Networks," *IEEE Trans. Neural Netw. Learn. Syst.*, vol. 28, no. 10, pp. 2243–2254, Oct. 2017.
[24] S. M. LaValle, "Rapidly-exploring random trees: A new tool for path planning," Dept. Comput. Sci., Iowa State Univ., Ames, IA, USA, Tech. Rep. TR98-11, 1998.
[25] M. W. Hannan and I. D. Walker, "Analysis and experiments with an elephant's trunk robot," *Adv. Robot.*, vol. 15, no. 8, pp. 847–858, Jan. 2001.
[26] Y. Masutani, T. Iwatsu, and F. Miyazaki, "Motion estimation of unknown rigid body under no external forces and moments," in *Proc. IEEE Int. Conf. Robot. Autom.*, San Diego, CA, USA, Dec. 2002, pp. 1066–1072.
[27] J. K. Thienel and R. M. Sanner, "Hubble space telescope angular velocity estimation during the robotic servicing mission," *AIAA J. Guid. Control Dyn.*, vol. 30, no. 1, pp. 29–34, Feb. 2007.
[28] Y. H. Dai, Y. Y. Lian, and G. Xie, "The mechanical arm of SIX-DoF obstacle avoidance path planning based on rapid-exploring random trees," *Tech. Autom. Appl.*, vol. 31, no. 10, pp. 31–37, 2012.

WENYA WAN received the B.S. degree in flight vehicle design and engineering from the School of Astronautics, Northwestern Polytechnical University (NPU), Xi'an, China, in 2016, where she is currently pursuing the Ph.D. degree with the National Key Laboratory of Aerospace Flight Dynamics. Her current research interests are in grasping planning and space flight dynamics and control.

CHONG SUN received the B.S. degree in flight vehicle design and engineering, the M.S. degree in flight mechanics, and the Ph.D. degree in astronautics engineering from Northwestern Polytechnical University (NPU), Xi'an, China, in 2010, 2013, and 2017, respectively.

Since 2017, he has been an Assistant Research Fellow with the School of Astronautics, NPU. His research interest is in space flight dynamics and control.

JIANPING YUAN received the B.S. degree in control and navigation, the M.S. degree in math and mechanics, and the Ph.D. degree in astronautics engineering from Northwestern Polytechnic University (NPU), Xi'an, China, in 1977, 1981, and 1985, respectively.

From 1988 to 1990, he was an Alexander von Humboldt Research Fellow with the Institute of Flight Control, Technical University of Braunschweig, Braunschweig, Germany. Since 1990, he has been a Professor with the School of Astronautics, NPU. His current research interest includes dynamics and control in space flight.